AGU PUBLICATIONS

JGR

Journal of Geophysical Research: Solid Earth

RESEARCH ARTICLE
10.1002/2017JB014273

Key Points:
- Seismic data confirm ridge propagation induced by increased melt supply due to increased fertility or upwelling of the asthenosphere
- Source of melt supply is migrating, ended a transform fault, and possibly stopped OCC formation
- The growth direction of the enhanced melt supply region is influenced by the distance to "colder" mantle zones

Correspondence to:
A. Dannowski,
adannowski@geomar.de

Citation:
Dannowski, A., Morgan, J. P., Grevemeyer, I., & Ranero, C. R. (2018). Enhanced mantle upwelling/melting caused segment propagation, oceanic core complex die off, and the death of a transform fault: The Mid-Atlantic Ridge at 21.5°N. *Journal of Geophysical Research: Solid Earth*, *123*. https://doi.org/10.1002/2017JB014273

Received 4 APR 2017
Accepted 20 JAN 2018
Accepted article online 24 JAN 2018

Enhanced Mantle Upwelling/Melting Caused Segment Propagation, Oceanic Core Complex Die Off, and the Death of a Transform Fault: The Mid-Atlantic Ridge at 21.5°N

A. Dannowski[1], J. P. Morgan[2], I. Grevemeyer[1], and C. R. Ranero[3,4]

[1]GEOMAR/Helmholtz-Centre for Ocean Research Kiel, Kiel, Germany, [2]Earth Sciences Department, Royal Holloway University of London, London, UK, [3]Barcelona Centre for Subsurface Imaging, Institut de Ciencias del Mar, Barcelona, Spain, [4]ICREA, Barcelona, Spain

Abstract Crustal structure provides the key to understand the interplay of magmatism and tectonism, while oceanic crust is constructed at Mid-Ocean Ridges (MORs). At slow spreading rates, magmatic processes dominate central areas of MOR segments, whereas segment ends are highly tectonized. The TAMMAR segment at the Mid-Atlantic Ridge (MAR) between 21°25′N and 22°N is a magmatically active segment. At ~4.5 Ma this segment started to propagate south, causing the termination of the transform fault at 21°40′N. This stopped long-lived detachment faulting and caused the migration of the ridge offset to the south. Here a segment center with a high magmatic budget has replaced a transform fault region with limited magma supply. We present results from seismic refraction profiles that mapped the crustal structure across the ridge crest of the TAMMAR segment. Seismic data yield crustal structure changes at the segment center as a function of melt supply. Seismic Layer 3 underwent profound changes in thickness and became rapidly thicker ~5 Ma. This correlates with the observed "Bull's Eye" gravimetric anomaly in that region. Our observations support a temporal change from thick lithosphere with oceanic core complex formation and transform faulting to thin lithosphere with focused mantle upwelling and segment growth. Temporal changes in crustal construction are connected to variations in the underlying mantle. We propose that there is a link between the neighboring segments at a larger scale within the asthenosphere, to form a long, highly magmatically active macrosegment, here called the TAMMAR-Kane Macrosegment.

1. Introduction

Mid-Ocean Ridges (MORs) exhibit different types and scales of segmentation (Macdonald et al., 1988) that can be classified according to their shape, size, and longevity. Generally, slow-spreading ridges are characterized by a well-developed axial valley bounded along axis by large transform faults or smaller ridge discontinuities (Macdonald et al., 1991). The typical segment length at the slow-spreading northern Mid-Atlantic Ridge (MAR) is generally less than 100 km (Sempéré et al., 1993; Smith et al., 2003). However, the segment length may vary through time (Gac et al., 2006; Gente et al., 1995) and some segments lengthen at the expense of their neighbors, leaving oblique discordant structures created by ridge propagation (Hey, 1977).

Active propagating ridges have been detected at all types of ridges, from slow- to fast-spreading rates and at large and small scales (e.g., Briais et al., 2002; Carbotte et al., 1991; Cormier & Macdonald, 1994; Gente et al., 1995; Hey, 1977; Hey et al., 1980, 1986; Kleinrock et al., 1997; Maia et al., 2016; Sempéré et al., 1995). In this study, we focus on the Mid-Atlantic Ridge at 21°30′N, where the TAMMAR segment (between 21°25′N and 22°N) is rapidly propagating southward (Gente et al., 1996). The off-axis trace left by the propagator in the last 4.5 Myr. can be easily followed even in satellite altimetry-derived gravity data (Sandwell & Smith, 1997). Gente et al. (1995) and Maia and Gente (1998) studied the propagating ridge (PR) segment by means of bathymetric, magnetic, and gravimetric data, while Gac et al. (2006) modeled the thermal evolution. The along-axis crustal structure of the TAMMAR segment (TS) has been described in a previous seismic ocean-bottom hydrophone study (Dannowski et al., 2011) (P02 in Figure 1a). The across-axis structure and the temporal evolution of the segment north of TAMMAR segment (TN) were studied in Dannowski et al. (2010) (P08 in Figure 1a). The southern tip of the TAMMAR segment and the kinematics of the deformation caused by the southward propagation were studied by Kahle et al. (2016) (P03 in Figure 1a).

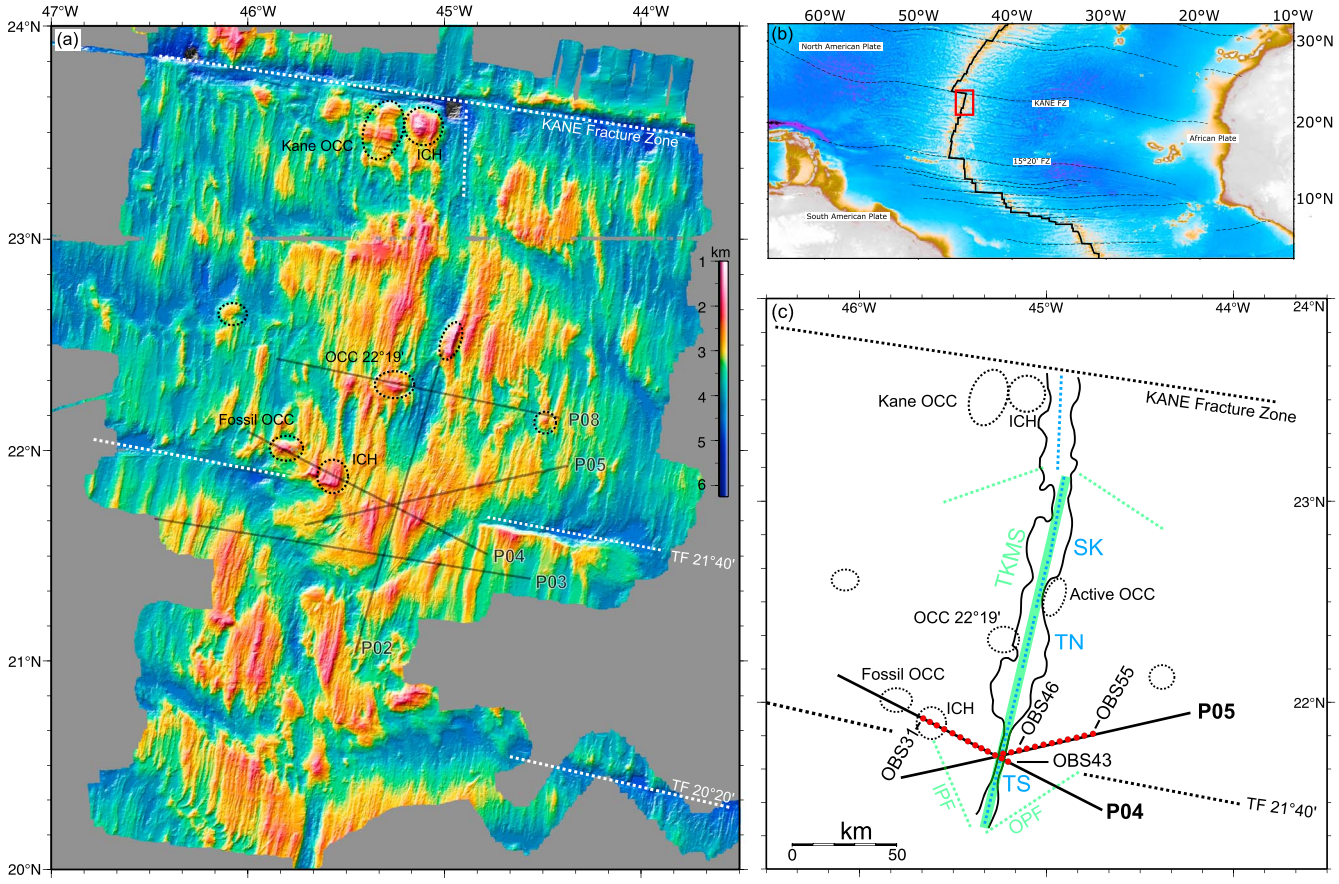

Figure 1. (a) Bathymetric map of the study area. White dotted lines mark offset discontinuities. Black dotted circles mark OCC's discussed in this study. Gray lines display the seismic lines from cruise M60-2. (b) Overview on the location of the study area along the MAR. (c) Major features discussed in this study (IPF and OPF = inner and outer pseudo fault; ICH = inside corner high; OCC = oceanic core complex; TS = TAMMAR segment, TN = TAMMAR-north segment, SK = southern Kane segment; and TKMS = TAMMAR-Kane Macrosegment). Red circles present the locations of the deployed OBH's. Blue dashed lines mark the three MAR segments within the TAMMAR-Kane Macrosegment (TKMS) that is shown with a green line. Green dotted lines show the off-axis traces of discontinuities.

A general feature of propagating ridge segments along the northern MAR is the southward trend of all propagating segments between the Azores hot spot and 26°30′N. South of 26°30′N they have propagated both north and south, splitting the ridge flanks into rhomb-shaped areas (Gente et al., 1995). Propagation rates appear to depend on the spreading rate of the ridge segments; thus, the faster the spreading rate of the spreading center, the higher the propagation rate (Morgan & Sandwell, 1994). The process of rift propagation generally involves the lengthening of the spreading segment at the expense of the adjacent segments (Gente et al., 1995). Several nonexclusive potential mechanisms have been proposed to describe active propagating ridges (PRs). This includes propagation down an along-ridge-axis topographic gradient (Morgan & Parmentier, 1985; Morgan & Sandwell, 1994), changes in the direction of seafloor spreading (Briais et al., 2002; Hey et al., 1980, 1988; Searle & Hey, 1983; Wilson et al., 1984), and crack propagation forces (Macdonald et al., 1991; Morgan & Parmentier, 1985). Proposed mechanisms related to changes in magmatic input include hot spots (Brozena & White, 1990; Schouten et al., 1987), tectonic extension due to changes in the magmatic input (Kleinrock et al., 1997), and increase in melt supply (Gente et al., 1995; Maia et al., 2016; Maia & Gente, 1998).

The evolution of the TAMMAR propagating ridge segment is expected to be connected to temporal variations in crustal production, as inferred from gravity field data (Maia & Gente, 1998). However, crustal thickness variations and density structure are underconstrained with gravity measurements and the inversion of the Mantle Bouger Anomaly (MBA) alone. Changes in crustal thickness and structures resulting from variations in accretion processes can be easily traced by seismic techniques. Seismic refraction and wide-angle

reflection data were acquired by the German R/V *Meteor* (M60/2) in December of 2003 and January of 2004. Here we report crustal thickness constraints on melt supply and melt distribution during ridge propagation and its temporal evolution. We study the macrostructure of the region between the 21°40′ transform and the Kane fracture zone to understand possible mechanisms that control ridge propagation in the study area.

2. Tectonic Settings

The region between 21.3° and 23.2°N, south of Kane fracture zone, is thought to be one of the most magmatic areas of the MAR (Gente et al., 1996; Thibaud et al., 1998). Maia and Gente (1998) and Cann et al. (2015) numbered the segments south of Kane fracture zone in different ways. We here refer to them as MG1-MG5 and C1-C5, respectively.

The region includes the TAMMAR segment (TS) (MG3/C5) that has propagated southward over the last 4.5 m.y (Gente et al., 1995). The southern TS segment boundary corresponds to a 40 km long offset at 21°20′N. However, in the north, the TS segment ends at a zero-offset discontinuity at 22°05′N and is terminated by a short less magmatically robust segment, here called the TAMMAR-NORTH (TN) segment (MG2/C4). In contrast to its neighboring segments, the TN segment is characterized by high seismicity (Smith et al., 2003) and existed for roughly 5 Myr (Gente et al., 1995). TN recently developed an oceanic core complex (OCC) in the center of the segment at 22°19′ on the western ridge flank. Interesting, in the north, the TN segment is bounded by another short zero-offset discontinuity to a segment with similar high seismicity (Smith et al., 2003) and thus probably similar low magmatic activity (C3), evolving an OCC on the eastern flank of the ridge axis, which is still under construction (Toomey et al., 1988). This short segment is bounded to the north by a highly magmatically active ridge segment (C2), which shows low seismicity (Smith et al., 2003) and propagated toward the north into the MG1/C1 segment immediately south of Kane fracture zone (Maia & Gente, 1998). As both segments (C3 and C2) are united in the off-axis area (Cann et al., 2015), we here refer to them as one segment and call it the Southern Kane (SK) segment (MG2/C2-C3).

In general, the average spreading rate of the segments south of Kane fracture zone is about 14 mm/yr to the west and 12 mm/yr to the east (Maia & Gente, 1998), while the MG1/C1 segment immediately south of the KANE fracture zone spreads at slightly slower rates (Gente et al., 1995; Maia & Gente, 1998).

The SK segment started its northward propagation already about 8 Ma (Figure 2a), at a similar propagation rate (~16 mm/yr) to the present-day TAMMAR segment. At about 5.5 Ma, SK propagation slowed but has persisted until the present with a uniform propagation rate. The northern segment does not leave such a prominent bathymetric record since there is only a small offset between the active propagating and doomed ridge axes. A short time (~1 Myr) after the SK segment slowed its propagation, the TS propagator began its southward propagation approximately 4.5 Ma (Gente et al., 1995), producing a prominent V-shaped wake in the lithosphere (Figures 1a and 2). The sharp linear wake on the eastern side was created by a constant propagation rate after a rapid initiation of propagation (Morgan & Sandwell, 1994), while the spreading rate has remained constant (Müller et al., 2008). For a slow-spreading ridge, like the MAR, the PR displays a remarkably fast propagation rate, propagating roughly 0.6 times the spreading rate. Both V-shaped structures (SK and TS) correspond to large mantle Bouger anomalies of up to −40 mGal, and thus, they are two of the largest anomalies along the MAR (Maia & Gente, 1998; Thibaud et al., 1998). Including the TN segment, they form a rhomb-shaped structure in seafloor relief (Figure 1c) (Gente et al., 1995).

Recognizing the propagation history of the area, there might be a link between all three segments (TS, TN, and SK) with their lithospheric segmentation that is expressed in mantle upwelling and the seafloor features described previously. We propose that there is a link between the segments at a larger scale within the asthenosphere, to form a long, highly magmatically active macrosegment, here called the TAMMAR-Kane Macrosegment (TKMS).

A perplexing feature is the breakthrough of the TKMS, at 21°40′N into a fossil transform fault (TF). This feature and related processes north and south along the MAR have been intensively studied by Gente et al. (1995) and Maia and Gente (1998) using magnetic and gravity data. The continuous structures of the fossil fault zone (Figures 1 and 2a) illustrate the stability of this spreading segment before recent propagation began. However, during early stages of propagation, this setting became unstable and the structures disappeared near the ridge axis. The V-shaped trace of the PR connects the ancient now inactive fracture zone with the

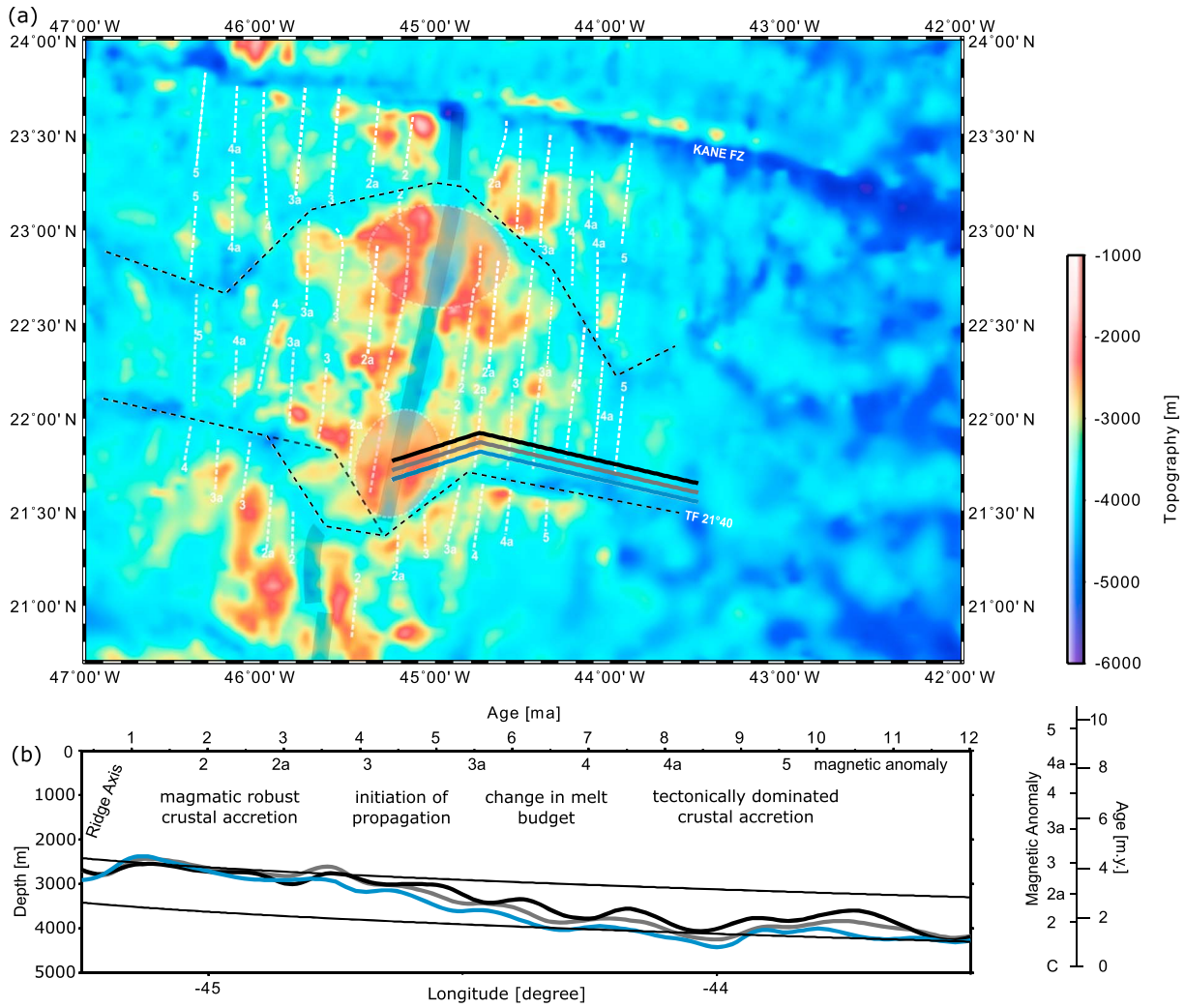

Figure 2. (a) Magnetic anomalies (Gente et al., 1995) (white lines) plotted on top of the bathymetry (Smith & Sandwell, 1997). Zones of negative MBA (Bull's Eye structures) (Maia & Gente, 1998) are schematically marked with shaded ellipsoids. The transparent gray stripe marks the present ridge axis. Black dashed lines illustrate the segment boundaries of the TAMMAR-KANE Macrosegment (TKMS). The gray, blue, and black lines mark the profiles compared in Figure 2b. (b) Seafloor depth with age compared to the cooling curves (Parsons & Sclater, 1977) for two cases of different deep segment centers.

present offset feature. During propagation, the present-day axial discontinuity has shortened in offset from about 50 km to its present-day 40 km. It is no longer a TF but instead has become a "sheared zone." While the eastern trace is a clear furrow, the western trace is a broader and tectonically disturbed area, which characterizes the patch of transferred lithosphere during the propagation.

3. Data Acquisition, Processing, and Analysis

Two active seismic refraction and wide-angle profiles were shot across the ridge axis of the Mid-Atlantic Ridge at 21.5°N (Figure 1). The experiment included a total of 25 ocean-bottom hydrophone (OBH) deployments. The two profiles P04 and P05 cross the ridge axis near the segment center. They have a length of 140 km each and give insights into the development of the segment center during the past 5 million years. The topography in this area is rugged. The quality of the data is good to excellent, providing clear crustal refraction branches (Pg) and crust-mantle boundary (Moho) reflections (PmP) (Figure 3). In addition, all deployed instruments provide clear mantle refraction phases (Pn). Gravity data were gained in an earlier experiment within the study area using a KSS30 Bodenseewerk gravimeter (Maia & Gente, 1998) (Figure 4).

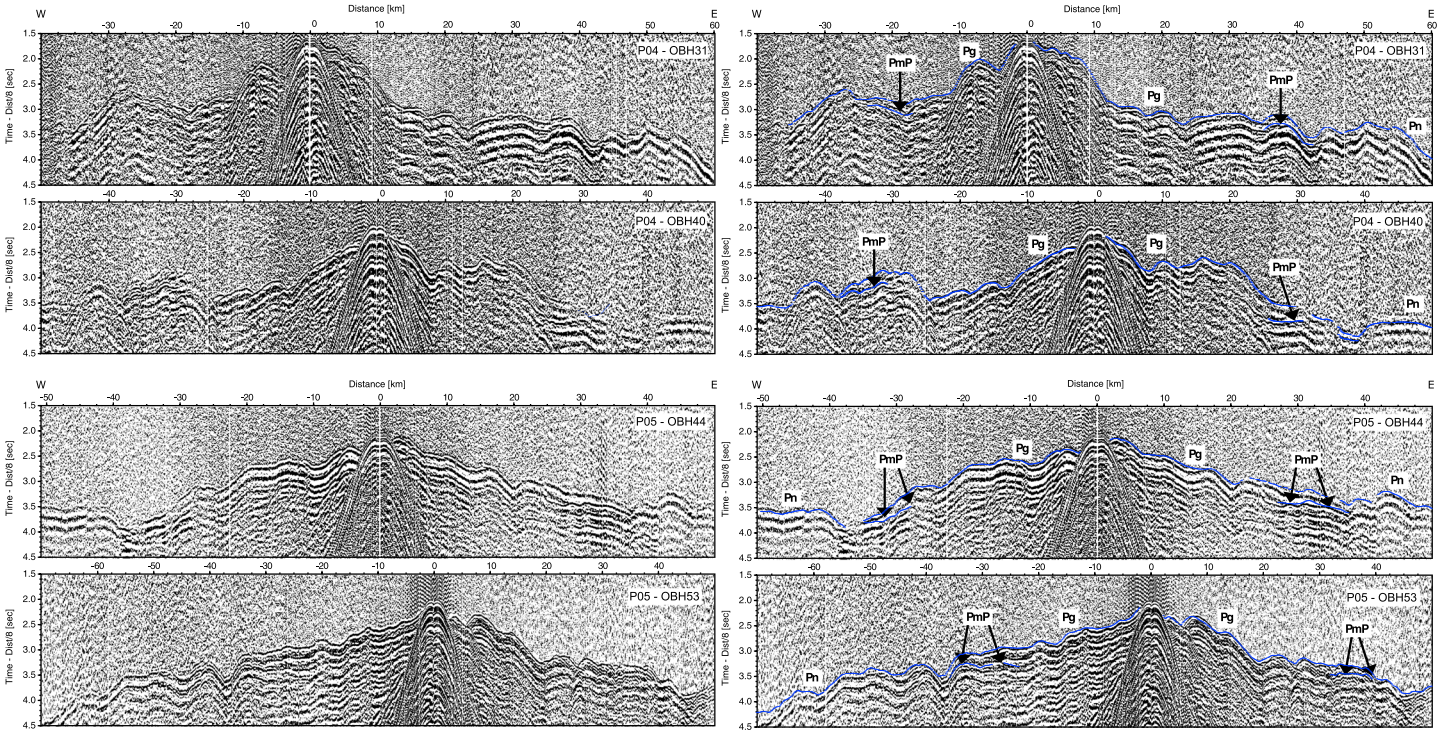

Figure 3. Hydrophone records for selected instruments: (left column) plain data after processing for two OBH records for each profile P04 and P05 and (right column) the calculated travel time picks from the final velocity model on top of the data. Phases are labeled with Pg = refracted crustal arrival, Pn = refracted mantle arrival, and PmP = reflected mantle arrival.

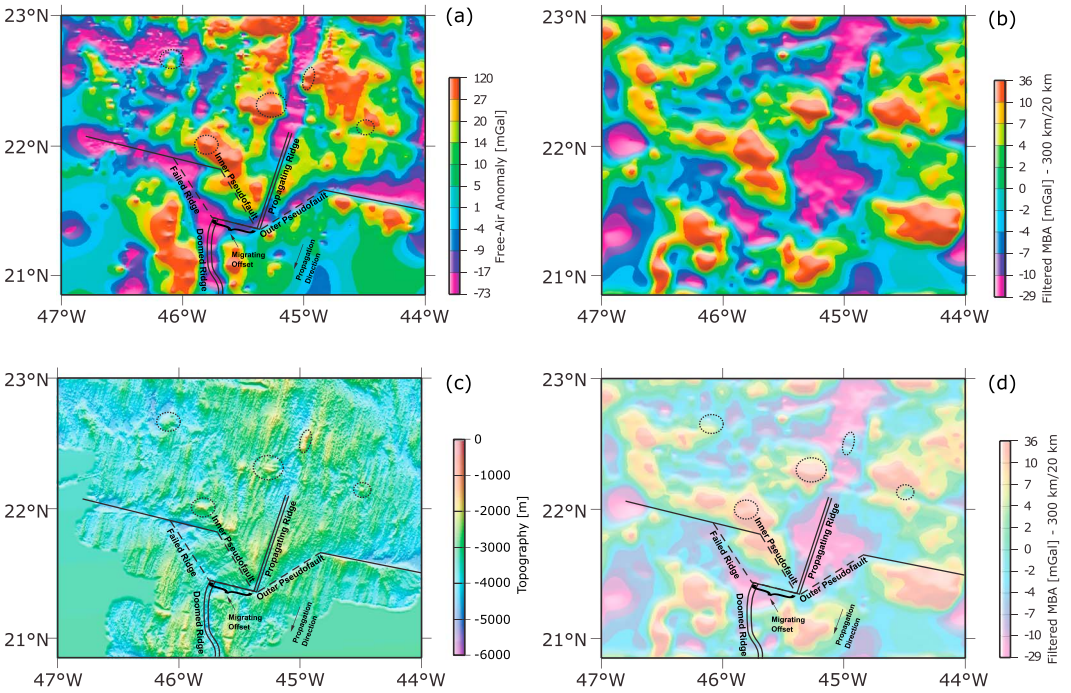

Figure 4. (a) Free-air gravity anomaly field (Maia & Gente, 1998). (b) Filtered MBA (300 km and 20 km for long and short wavelengths) removing topography of seafloor and the crust-mantle boundary, assuming a 6 km thick crust. (c) Bathymetry overlain by the tectonic features of the study area. (d) Tectonic features on top of the filtered MBA for comparison with bathymetry.

3.1. Data Input and Processing

As seismic source, we used two 32-liter Bolt Inc. airguns (~3,900 cubic inch) operating at a pressure of 130 bar and towed at a depth of 10 m with a shot interval of 60 s over both profiles. Having an average ship velocity of 4 knots (~2 m/s) yields a trace spacing of approximately 120 m and ~1,100 shots per profile.

The data were continuously recorded with a sampling rate of either 200 or 250 Hz. After the instrument recovery, the data were played back and split into single shot records as a receiver gather in SEG-Y format. Based on GPS and ship's navigation system, shot locations were corrected for the offset between the GPS-antenna and the airgun array. Receiver positions on the seafloor were relocated using direct water wave travel times. All data loggers were synchronized with a GPS-time signal before and after recording to correct for a possible linear clock drift. To enhance the signal-to-noise ratio, we applied deconvolution (Wiener, 1949) and an Ormsby frequency filter. The time- and offset-variant band-pass filter moves toward lower frequencies as time and offset increase. Data examples are given in Figure 3.

3.2. Travel Time Picking

Most of the stations show a high signal-to-noise ratio that allowed a clear identification of *P* wave arrivals. Three distinct crustal arrivals were identified: a high-amplitude refracted phase from Layer 2 (Whitmarsh, 1978) that occurs to ranges of ~15 km (Pg), a lower amplitude refracted phase from Layer 3 (White et al., 1992) that continues to ranges of up to 35 km (Pg), and a high-amplitude wide-angle reflection from the crust-mantle boundary (Moho) observed on some stations as a distinct second arrival at 20–40 km range (PmP). We could observe refracted mantle phases (Pn) even at large offsets of up to 70 km, partly limited by the profile length. Primary phases at the onset of the first positive amplitude peak from the crust and the mantle and secondary arrivals were manually picked. Figure 3 contains seismic sections as data examples and travel time misfits for two stations from each profile. The pick uncertainty has been estimated to range between 20 and 70 ms. Larger uncertainties were assigned to noisier data, usually for crustal and mantle arrivals with smaller amplitudes recorded at larger source-receiver offsets.

It is interesting to note that the data are strongly affected by the steep bathymetry that obscures PmP arrivals; thus, the PmP phase does not appear at all stations as a clear arrival with strong amplitudes. This feature is perhaps also caused by variation in the velocity contrast at the crust-mantle boundary. Short branches of PmP arrivals were identified and picked where possible using the forward and back shots and the multiples at adjacent stations. The critical distance for wide-angle reflections of the seismic Moho (PmP) along the profiles ranges at about 30–40 km.

3.3. Travel Time Tomography and Modeling Strategy

Velocity models for each profile were determined using the travel time tomography technique of Korenaga et al. (2000), which jointly inverts refracted and wide-angle reflected travel times for a two-dimensional velocity structure. The geometry of the Moho is constrained to a floating reflector, an approach, where the depth of single reflector nodes is updated freely without changing adjacent velocity nodes. To achieve an accurate forward solution, the hybrid ray-tracing scheme is based on the graph method (Moser, 1991). Additional local ray-bending refinement (Moser et al., 1992) was employed; smoothing and damping constraints were used to regularize the iterative inversion. The velocity model is parameterized on a sheared mesh with parallelogram shaped cells "hanging" beneath the seafloor. The velocity field is continuous everywhere and is interpolated within each cell. The seafloor was parameterized at a spacing of 1 km, while the regular grid has grid cells with a uniform horizontal spacing of 200 m and a vertical spacing increasing from 50 to 170 m. The weighting parameters for velocity and depth smoothing and damping are the same for both profiles, with 40 and 20 for velocity and depth, respectively. A weighting factor of $w = 1$ was used for weighting the depth and the velocity nodes equally. A larger weighting factor should lead to larger depth perturbations (Korenaga et al., 2000). With respect to resolution and preliminary parameter tests, we chose the following values for the correlation length: the horizontal correlation length for velocity nodes ranges from 1 km at the seafloor to 5 km at the bottom, and the vertical correlation length varies from 0.5 km to 3 km (top to bottom of the entire model room).

The modeling approach consisted of several steps. First, 1-D modeling of single stations from the ends and the center of each profile was performed to derive initial two-dimensional velocity structure models. Next, downward stripping of the layers was carried out by first inverting for the upper crustal arrivals and then

inverting for all deeper crustal arrivals. Once derived, first arrival picks of larger offsets were added. In a further step, the Moho depth was determined from the PmP arrivals (where they have been observed). Finally, Pn arrivals were included to obtain the uppermost mantle velocity structures. During each stage a broad model space was tested to verify the model uncertainties.

3.4. Gravity Data and Modeling

To provide an estimation of the subsurface density structure and depth of Moho, free-air gravity anomalies across the ridge axis were investigated, in conjunction with a well-constrained seismic velocity model. Since there is a trade-off between velocity and layer thickness, the depth of the Moho partly depends on the starting model. Thus, different solutions can fit the seismic travel times. However, gravity data, as a second data set, can help to minimize the nonuniqueness of the seismic model.

Free-air gravity anomaly data (Maia & Gente, 1998) are shown in Figure 4a. By removing the effect of the density contrast at the seafloor (assuming no sediment cover) and at the crust-mantle boundary (assuming 6 km thick crust), the mantle Bouguer anomaly was calculated. Filters for the long wavelengths (300 km) and short wavelengths (20 km) were applied to produce the filtered MBA image in Figure 4b. From the free-air gravity anomaly field (Figure 4a), data were extracted along the seismic lines. Initially, based on the seismic results, a 2-D density grid was created applying the empirical V_p-density relationships of Carlson and Herrick (1990) and Birch (1961) (for diabase, gabbro, and eclogite) for upper crust and lower crust, respectively (Korenaga et al., 2001). Densities at the seafloor started at 2.4 g/cm^3 (Stevenson et al., 1994) and reached 2.8 g/cm^3 (near the 6 km/s contour). Above the seismic Moho an initial density of 3.05 g/cm^3 was chosen and the upper mantle had an initial density of 3.3 g/cm^3. The model has a total depth of 20 km. The initial interfaces were adopted from the seismic velocity model. Forward gravity modeling was applied until the misfit of the data was reasonable small (Figure 5c). The depth of the crust-mantle boundary at the model ends has poor seismic constraints, and it was modified during the gravity forward modeling. The initial mantle density of 3.3 g/cm^3 was reduced to 3.25 g/cm^3 beneath the ridge axis to obtain a reasonable fit between the calculated and observed gravity data. The increase in mantle density with distance from the ridge axis agrees with the expected thermal cooling of the lithosphere. Lin et al. (1990) describe the temperature effect on the density by $\Delta\rho = -\rho_0 \times \alpha \times \Delta T$, where ρ_0 is a reference density, α is the coefficient of thermal expansion ($\alpha = 3.4 \times 10^{-5}$°C^{-1}), and ΔT is the excess in mantle temperature. Across the ridge axis, we assume lithospheric cooling as the major source for density increase. Based on the gravity modeling for the TAMMAR segment (Figure 5c), we observe a ΔT of ~450°C between the ridge axis and about 70 km off axis. This is comparable to the temperature differences observed by Lin et al. (1990) for the MAR at 29.5°N, a similar magmatic robust ridge segment.

4. Results

In general, V_p models (Figures 5a and 5b) show an increasing velocity with depth at different gradients. We define three layers mainly based on changes in velocity gradient. The uppermost layer is interpreted as seismic Layer 2 forming the upper crust typically inferred to be composed of basalts and dolerites. It is characterized by a high-velocity gradient and a rather constant thickness. Velocities of 2.9 to 3.4 km/s have been observed close to the seafloor (faster with distance to the ridge axis); the bottom of this layer is indicated by the 6.0 km/s isoline. Below this, an abrupt change occurs to a gentle velocity gradient. The velocity gradient changes again at ~7.1 km/s to a higher gradient forming the base of the second model layer. The low-velocity gradient lower crustal layer is interpreted as Layer 3, typically inferred to be gabbroic in nature. The base of the crust is underlain by a transition zone with velocity $>$ ~7.3 km/s that possibly represent mantle material. This transition zone is poorly sampled in seismic records; however, the high-velocity gradient supports a change in lithology from crust to peridotitic mantle. The crust-to-mantle transition zone is marked by a rapid change in seismic velocities from about 7.1 to 7.4 km/s within 1 km. The uppermost part of the mantle is poorly constrained by travel time tomography. It shows velocities of 7.3 km/s near the MAR axis to 7.7 km/s at the MAR flanks on both profiles. However, there are few crossing rays and the majority of rays travel as head waves along the boundary. Thus, the inferred mantle velocities have higher uncertainties. The depth and shape of the seismic Moho are verified by gravity modeling (Figure 5c). While the upper mantle shows lower densities at the ridge axis, densities increase with offset similarly to seismic *P* wave velocities.

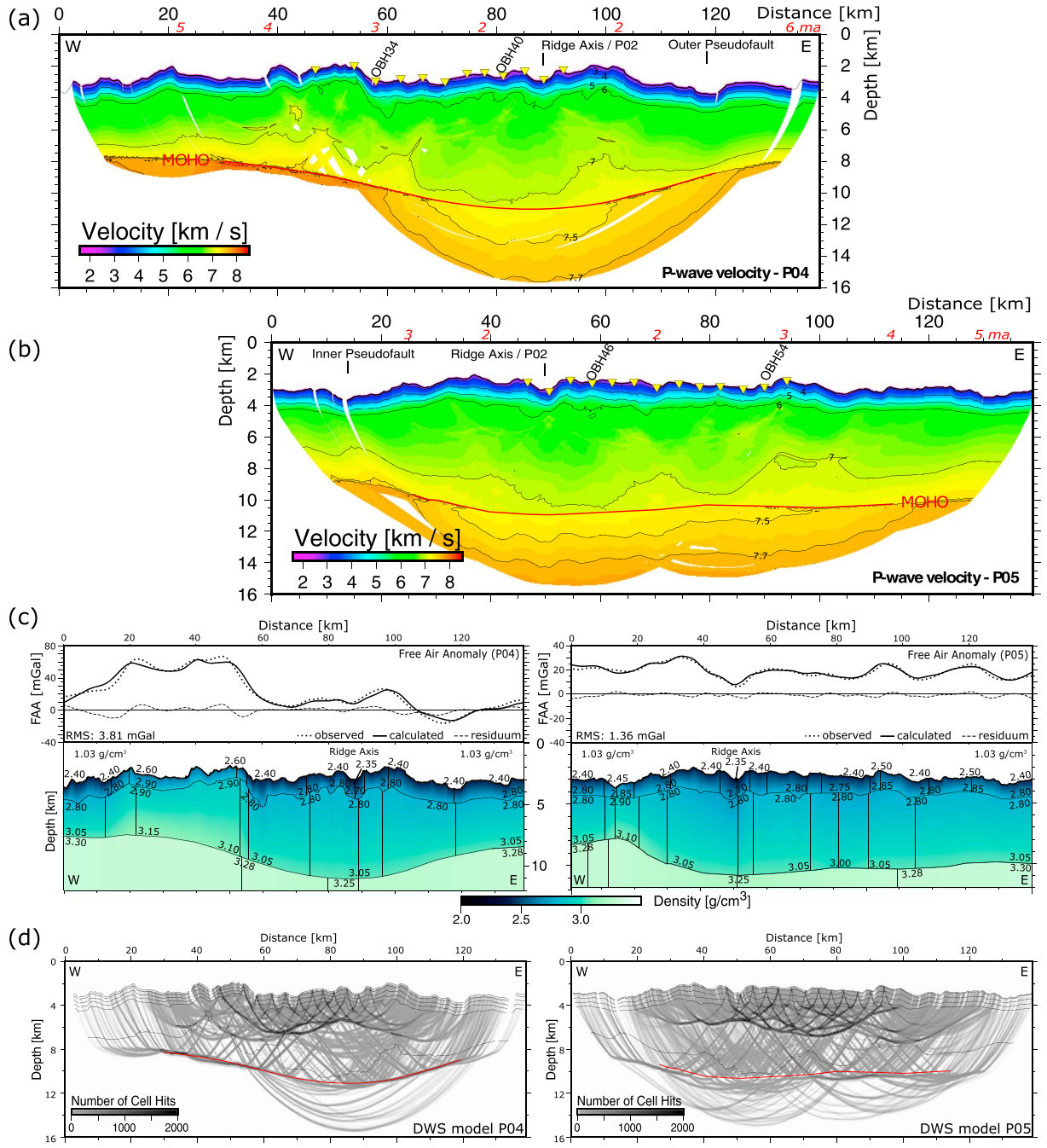

Figure 5. Final velocity models for (a) P04 and (b) P05. Yellow triangles mark the OBS positions. Red numbers above the frame represent plate age (Gente et al., 1995). (c) Gravity modeling for profiles P04 and P05. Upper panel shows the fit from observed (Maia & Gente, 1998) and calculated gravity data. Numbers mark densities from the crust and mantle. Densities directly above the seafloor belong to the top of crust. (d) Derivative weight sum and demonstration of raypaths for profiles P04 and P05.

High velocities at the seafloor indicate the absence of sedimentary coverage. The observed increasing Layer 2 velocity with crustal age is a common phenomenon that is thought to be related to hydrothermal precipitation of secondary alteration products into open pore spaces and cracks, decreasing the porosity and hence increasing seismic velocities (e.g., Carlson, 1998; Grevemeyer & Weigel, 1996, 1997). The *P* wave velocity of Layer 2 is believed to reflect the porosity structure of this basaltic layer. The decrease in porosity with depth is inferred to be caused by decreased pore space with depth through crack closure with increasing confining

pressure (Carlson & Herrick, 1990; Shearer, 1988) and possibly faster rates of precipitation from warmer fluids at depth, hence increases in seismic velocity to ~6 km/s 1.5–2 km below the seafloor. Both profiles show a rather constant thickness of Layer 2.

It is interesting that although P04 and P05 are not perpendicular to the ridge axis, at the intersections with P02 (Dannowski et al., 2011), the measured along-ridge *P* wave velocities show slightly higher values than cross-ridge velocities, indicating anisotropy within the entire crust. Tomography results show velocities of ~3.2 km/s along axis in contrast to ~2.9 km/s across the ridge axis at the seafloor. At Moho depth, along-axis velocities of ~7.4 km/s are observed in contrast to ~7.1 km/s velocities on the ridge crossing profiles. The observed anisotropy can be explained by ridge axis parallel aligned faults and fissures.

The *P* wave velocity structures near the ridge axis fit well with results of similar magmatic active segments, for example, OH-1 (Canales et al., 2000) and Lucky Strike (Seher et al., 2010). These segments show a rapid increase (1.5 s^{-1}) in seismic velocities in the upper crust. From ~2 km below the seafloor, seismic velocities increase at a lower gradient (0.5 s^{-1}) with depth. The crustal thickness of up to 8 km is similar at all three segments. While Lucky Strike shows evidence for a magma chamber at intermediate depth (3–3.5 km), there are no indications of a similar feature in the seismic data at the TAMMAR segment.

4.1. Seismic Tomography: P04

The bathymetry along profile p04 suggests a tectonically disturbed, abruptly changing crustal structure that crosses different tectonic units (Figures 1 and 5). The profile crosses the outer pseudofault of the propagator in the east (km 120), a fossil inside corner high (ICH), perhaps indicative of an OCC (although its morphology would not be typical) at km ~50, and an older OCC at km 20. The OCC at km 20 is not covered by stations; thus, its crustal structure is not well resolved, and the modeling results strongly depend on the starting models. The gravity data (Figure 5c) imaged comparatively thinner crust for this part of the model, in agreement with the inferred seismic velocities.

The velocity model indicates a strong lateral variation in velocity close to the seafloor, varying from 2.9 km/s in the central valley to 3.4 km/s at the flanking rift mountains. The upper crust between km 45–55 is faster, reaching velocities up to 3.6 km/s at the seafloor. The velocities at greater depth (>7 km/s) are "pulled-up" to 4 km below the seafloor between km 55 and 65. This structure, interpreted as an inside corner high (ICH), is possibly connected to a deep-cutting fault. Here the presence of crustal rocks that have been transported upward from greater depths can explain the higher velocities within the crust. Similar structures are imaged on the OCC farther west at km 40, and the 7 km/s contour is elevated between km 45 and 50. Gravity supports the interpretation of a comparatively thinner crust, as this region has a positive gravity anomaly (Figure 5c). Directly east of the dome-shaped ICH (km 60), the upper crust shows a zone of lower velocity. Farther east, the velocities at the seafloor decrease and reach a minimum at the ridge axis (km 90), while the crustal thickness of Layer 2 remains almost constant. In contrast, a large variation in crustal thickness is observed within the lower crust. Summing up both portions of the crust, the total crustal thickness decreases with distance from the ridge axis, from ~8 km to ~5.5 km at km 35. There is an abrupt increase in crustal thickness of about 2 km between km 40 and 70.

The crust on the eastern end of the profile is thinner. Although the profile segment between km 100 and 140 is not covered by stations, the gravity results (Figure 5c) support a thin crust with ~5 km thickness. At km 120 the outer pseudofault is crossed, and farther east the seismic line covers the southern segment with roughly 3 Myr older crust. Seismic velocities within Layer 3 vary little along the profile. Kahle et al. (2016) found a similar crustal thickness of ~5.5 km along P03, which crosses the outer pseudofault farther south and closer to the ridge axis. While Layer 2 thins a few hundred meters, the main portion of crustal thinning is expressed in Layer 3.

The ray coverage (Figure 5d) is good beneath the region covered by stations down to Moho depth, while rays do not penetrate as deep at the western edge. Along P04 a total of 5,433 crustal refractions, 917 mantle reflections, and 2,989 mantle refractions have been picked by hand. The model converged to X^2 = 1.35 and a RMS misfit of 48 ms after eight iterations, which implies a rapid convergence from the starting models to a reliable 2-D velocity structure. These results are further constrained by and consistent with 2-D gravity modeling (Figure 5c).

4.2. Seismic Tomography: P05

The bathymetry along P05 indicates a comparatively tectonically undisturbed crustal structure (Figure 1). However, Layer 2 along this profile is very similar to the structure found along P04 and is characterized by a high-velocity gradient and a quasi-uniform thickness (Figure 5b). Upper crust velocity rises with age from 2.9 km/s in the central valley to 3.4 km/s at 40 km distance. Layer 3 thins with distance from the ridge axis, from ~7 km to ~6 km. This gradual thinning starts at the ridge axis (km 50) and extends to km ~85. Farther east, the crustal thickness remains fairly constant. However, this profile segment is not covered by stations; thus, its velocity model strongly depends on the starting model. Gravity modeling (Figure 5c) supports a slow decrease in crustal thickness toward the east on the eastern part of P05. Layer 3 *P* wave velocities increase gently from ~6 km/s to 7.0–7.2 km/s at its base. Near the Moho, crustal velocities increase rapidly from 7.1–7.3 km/s to 7.7 km/s.

The velocity structure for profile P05 at the ridge axis fits well to the results of profile P04 (Figure 5a). Along P05 a total of 12,787 picks with 6,802 picks from crustal first arrivals (Pg), 4,318 mantle first arrivals (Pn), and 1,667 mantle reflections (PmP) have been picked by hand. The model converged to $X^2 = 1.50$ and a misfit of 52 ms after eight iterations, indicating a rapid convergence from the starting model to a reliable 2-D velocity structure. The results are supported by 2-D gravity modeling (Figure 5c). Fits of the calculated travel times to seismic records are shown in Figures 3e–3h. The ray coverage (Figure 5d) is very good beneath the region covered by stations down to Moho. A number of crossing rays penetrate the mantle; however, the resolution is still quite poor, which can be explained by the short offsets between the OBS stations that were only distributed in the center of the profile.

5. Discussion

5.1. Evolution of the TAMMAR Segment

The two profiles follow the fossil segment center of the southward propagating TAMMAR segment (Figure 1) and thus constrain the evolution of this segment center over the past 6 million years. The eastern side imaged by profile P05 covers a tectonically undisturbed part. On the eastern flank, it shows a slowly increasing crustal thickness since 5 Ma. The western flank of the axial valley (profile P04) shows a stronger variation in crustal thickness over the past 6 Myr. This implies a uniform increase in melt supply during the past 5 Myr and asymmetric crustal construction with thicker crust at the eastern side of the ridge axis for ages $>$5 Ma. Robust magmatic accretion to the eastern flank is supported by the bathymetry and gravimetric modeling (Figure 5c). The seafloor exhibits comparatively shallower elongated abyssal hills with small faults extending across the entire segment eastern flank.

The gray line in the bathymetry map of Figure 2a follows the segment center within the past 3 Myr since magnetic anomaly 2a. The bathymetry indicates that the segment center is migrating southward, however, at a slower rate than the propagation rate of the southern segment tip. This means that the location of maximum melt supply (and mantle upwelling?) is migrating southward, and thus, the segment end should also move southward. The difference between the propagation rate and the migration rate of the segment center is interpreted to be a result of increased melt supply causing the growth of the segment. Crustal thickening during segment growth (Figures 5a and 5b) implies that the magmatic budget became larger over time. The seismic results report crustal thickening of 2 km over a period of 2 Myr (km 40 to km 70), confirming the findings of Maia and Gente (1998). They observed crustal thickening of up to 2.5 km in the segment center based on residual gravity analysis. Figure 2b shows calculated cooling curves (Parsons & Sclater, 1977) for the seafloor depth-age dependence for two cases. These curves can be compared to measured seafloor depths. The upper smooth seafloor depth curve represents the theoretical depth of the actual axial valley. The lower smooth depth curve was calculated for a 1 km deeper axial valley, which would represent a more strongly tectonic phase of seafloor production. While the younger depth data fit the upper curve better, the older depth data fit the lower curve better. Thus, a secular change in the magma supply can be inferred, indicating a change from an earlier tectonically dominated phase of plate separation to a recent more magmatically dominated phase.

The fossil oceanic core complex on the western side of the ridge axis at 22°N/45.8°W (Figure 1) is a witness to a period of tectonically dominated seafloor spreading. Buck et al. (2005) and Tucholke et al. (2008) proposed

that detachment faulting occurs within certain limits of magmatism, specified by the fraction of the plate separation rate that is taken up by melt accretion *M*. This indicates that the total extension was accommodated between 30 and 50% by magmatic accretion, before the lengthening of the TAMMAR segment started. At about 5.5 Ma detachment faulting stopped. However, ridge crest segmentation did not change at this stage. Instead, magmatic construction was enhanced; for example, the melt accretion fraction increased to $M > 0.5$. The V_p model (Figure 5a) shows a slight increase in crustal thickness during the following 1 Myr. During both phases crust was accreted asymmetrically with more crustal material added to the eastern side, while spreading rate stays constant. At the same time the northward propagating SK segment slowed down its propagation. At roughly 4.5 Ma on the western side, the crustal thickness rapidly increased by 1 km (over 12 km of distance or ~1 Ma). At this time segment propagation started, as is also indicated by the change in the seafloor topography (Figure 2b). Subsequently, crustal thickness increased toward its present ~8 km of thickness and evolved to more symmetric crustal accretion to both sides of the magmatically robust ridge axis, while half spreading rates stay asymmetric (14 mm/yr west and 12 mm/yr east (Maia & Gente, 1998)).

The spatial pattern of the mantle Bouguer anomaly (MBA) along the TKMS (Maia & Gente, 1998) (Figure 4b) is consistent with these seismic observations, as are observations on a similar ridge configuration by Tolstoy et al. (1993) at the MAR 33°S. A negative MBA ("Bull's Eye" structure in 3-D) represents thick crust. Figure 2a shows a generalized topography that coincides with the two propagators. Topography and MBA indicate thick crust at both segments, TS and SK.

5.2. Lifecycle of Segment Propagation

A sudden increase in melt supply may mobilize dikes to propagate long distances laterally. Dikes preferentially penetrate into the direction where the tectonic stresses adjacent to the magma chamber are lowest (e.g., Buck et al., 2006). With increasing crustal thickness, the lower crust becomes more ductile, which makes lateral migration of the lower crust easier. The increasing crustal thickness over the last 4.5 Myr (Figures 5a and 5b) can be interpreted to be linked to such an increase of magma supply. In addition, the segment center has migrated southward, which indicates that the most magmatically robust region of accretion is slowly migrating southward. The migration speed of this magmatically robust region is slower than that of ridge propagation (Figure 2a). Because of this, we interpret that the source of ridge propagation related to the TKMS must have its origin in the underlying mantle.

Figure 2a shows the magnetic anomalies over a generalized bathymetry overlaid with two shaded ellipsoids roughly marking the extent of negative MBA anomalies of the SK and TS segments. Within a short time (~2.5 Myr) we observe two events of ridge propagation having their origin in mantle upwelling. As the first event undergoes a change, the second propagation event starts. We propose a connection between both events in the melting zone and group the segments expressed in the seafloor (TS, TN, and SK), to be at a larger scale the TAMMAR-KANE Macrosegment. Figure 6 sketches an idealized evolution of the area between the Kane fracture zone in the north and the southern ridge tip of the TAMMAR segment since 8 Ma. This interpretation is based on the observations in this study combined with earlier findings from previous studies in this region (Dannowski et al., 2011; Gente et al., 1995; Maia & Gente, 1998; Smith et al., 2003). Figure 6 illustrates three possible stages in the macrosegment's evolution induced by increasing melt supply. We start our sketch at magnetic anomaly 4a where the northern SK segment began to propagate northward (Figure 2). The high melt productivity zone under the ridge axis (Figure 6c) grows, due to increased temperature and/or possible changes in composition/fertility (Niu et al., 2001; Wilson et al., 2013). Increased melt productivity is linked to increased upwelling of the mantle in the northern segment. The emplacement of new oceanic crust is limited by spreading rate ($M = 1$); hence, additional material expands along axis (Gac et al., 2006) and spreading center parallel (Cushman et al., 2004). In the beginning of that process, the Kane transform fault may have been far enough away from the segment center so the hot zone had room to expand northward, while the southern smaller transform provided restricted room for expansion. At roughly 5.5 Ma propagation of the northern segment slowed and almost stopped. Possibly the older and thicker lithosphere north of the Kane transform became a barrier for the extension of the growing hot zone, so that the migration of the upwelling zone nearly stopped. As a consequence, the still increasing melt supply at constant spreading rate led to the expansion of the high productivity zone toward the south. The magmatic budget within the TAMMAR segment increased, and detachment faulting stopped. The transform at 21°40′, south of the TAMMAR segment, because of its much smaller offset, was a weaker barrier to along-axis growth than the

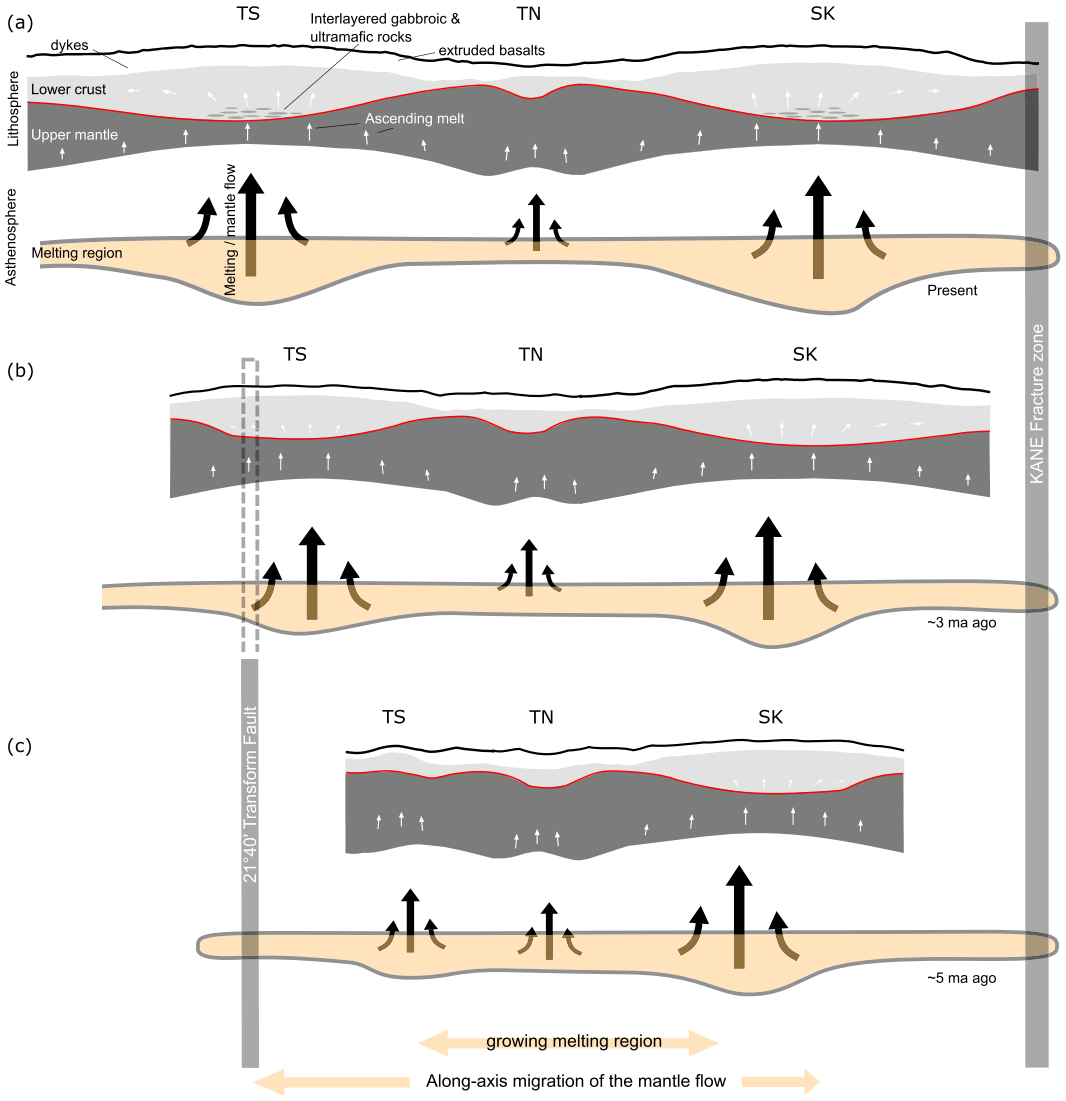

Figure 6. Idealized sketch of the evolution of the TAMMAR-Kane Macrosegment (TKMS). Present state is shown at the top.

Kane transform fault. About 4.5 Ma the segment "broke through" this transform offset (Figure 6b). Until present the TAMMAR segment is still growing southward, while the SK segment seems to have stopped its northward propagation (Figure 6a). The marked negative MBA (Figure 2a) partially overlies with elevated features that have been interpreted as OCC structures by Cann et al. (2015). If this assumption is right, we might see a change from magmatic dominated crustal accretion to OCC formation after mantle upwelling has stopped increasing at the northern end of the TKMS.

Several basic questions remain unanswered in this partial explanation. How long will the TAMMAR segment propagate? As long as its magmatic budget is rising, it probably will continue to extend. However, lateral dike propagation is limited by the ability of material to flow along axis to the dike tips, and the ease of lateral lower crustal flow will depend on the thermal structure of the section it flows "through." In principle, if the crust is still thickening while it can undergo significant along-axis flow, then it should become even more ductile and flow even more easily along axis. Nowadays, the TAMMAR segment is one of the longest segments along the MAR—perhaps due to this larger component of along-axis ductile flow? Will the segment center (the center of local mantle upwelling) continue to migrate toward the south even after the segment stops its expansion? Or would a reduction in segment melt supply suddenly stop, or even reverse, propagation and ridge migration?

5.3. Oceanic Core Complex Die Off and Transform Termination

Between the Kane transform fault and the TF at 21°40′ a number of oceanic core complexes or similar looking dome-shaped features can be observed. Most of them are situated west of the ridge axis (Figure 1) (Cann et al., 2015). The Kane OCC has been studied by several methods in the recent past (i.e., Canales, 2010; Dick et al., 2008; Karson, 1999). We want to highlight the OCC-like structures in the center of the TAMMAR-Kane macrosegment. The OCC at 22°40′ east of the ridge axis (Toomey et al., 1988) is still active. From bathymetry and the calculated MBA (Gente et al., 1995) (Figures 1a, 2, and 4) we observe that the OCC at 22°19′ west of the axial valley developed roughly 2 Ma (anomaly 2) (Dannowski et al., 2010). A third dome-shaped feature, interpreted to be an OCC, appears at 22°40′N at roughly 8 Myr (approximately anomaly 4a) on the western ridge flank. Further, however, less prominent on the eastern ridge flank, we interpret a feature at 22°10′N close to magnetic anomaly 3a (~5.5 Myr old) as an OCC. These observed ancient OCCs formed over a relatively short periods with detachment faulting within 1 to 2 Myr, which would favor rather low local melt supply (Cheadle & Grimes, 2010). The question remains whether the asymmetry in spreading rate, with a higher rate to the west, favors OCC formation to the faster-spreading side (Cann et al., 2015).

Interestingly, except for the OCC connected to the southern segment's end, the other four OCC structures developed in the macrosegment's center since 8 Ma (Figure 1a) to both sides of the ridge axis. The youngest OCC was created within the segment center of the TN segment (Figure 1c). The center of the TKMS seems to have a very stable history. It stayed within a certain level of low magmatic budget with $0.3 < M < 0.5$ and possibly alternating OCC formation to both sides of the ridge axis. The present wide shape of the axial valley hints to a starved melt supply ($M < 0.3$) and thus a tectonically dominant phase of plate extension. Perhaps, this is a consequence of the divergent migrating segment centers of the TS and the SK segments and their mantle upwelling regions. This leads to the question of what will happen to the center of the TKMS as the higher magma productivity zones continue to separate.

In contrast, the ICH at 21°40′ TF, north of the inner pseudofault at P04 (Figure 1a), looks similar to Atlantis Massif (Blackman et al., 2009). Here detachment faulting appears to have stopped by exceeding the upper limits of melt supply ($M > 0.5$) for a "stable" OCC configuration. This fault did not develop into an exhumed low-angle OCC (Figure 5a, KM ~55), perhaps because fault motions died before extension could progress to this stage. The segment end at this 50 km offset discontinuity was slowly replaced by the growing segment center, due to the southward migration of mantle upwelling beneath the TAMMAR segment. Thus, the migration of the melting region caused a change in the fundamental mode of spreading from a faulting mode to a volcanic mode and is what ultimately terminated the transform fault at 21°40′N. Terminating a transform fault in this way is a rarely observed process. Transform faults are very stable systems that often exist for long periods of time. One proposed mechanism to modify or terminate them is to change the direction of spreading (Menard & Atwater, 1968). However, here bathymetric data do not imply a significant change in spreading direction at ~5 Ma.

Few examples exist of the natural variability of melt supply to mid-ocean ridges. Analysis of dredge samples of exposed mantle rocks along a large equatorial transform of the MAR support an ~3–4 Myr long oscillations in the degree of mantle melting, related to upwelling patterns at slow-intermediate spreading rates (Bonatti et al., 2003). Similarly, regional seismic studies mapping relative variations in thickness of fast-spreading crust in the Pacific based on two-way travel time measurements (Ranero et al., 1997) support 2–3 Myr. long oscillations in melt production (Reston et al., 1999). A time-and-space variable degree of mantle melting would yield localized segments of enhanced crustal formation, triggering the development of melt-rich propagating ridges and abrupt variations in crustal architecture, including the abrupt abandonment of core complex faulting.

6. Conclusions

The MAR between the Kane transform fault and the 21°40′ TF can be divided into four ridge segments; the southern three form an intercommunicating macrosegment (the TKMS). This macrosegment has grown between 8 Myr and the present by ridge propagation at both its ends, creating a rhomb-shaped structure in the regional seafloor relief.

The crustal thickness within the TAMMAR segment center has increased over the past 5 million years from 5 km to 7 km at the present ridge axis. At the same time an increase in negative MBA is observed, which created a so-called Bull's Eye structure in 3-D. The trapezoid-shape of the Bull's Eye and the along-axis thickening of crust with thicker crust at the southern segment end compared to the northern end of the TAMMAR segment emphasize the role of stronger along-ridge melt supply (and the center of mantle upwelling) migrating toward the south. The appearance of mantle upwelling seems to have coincided with the onset of propagation ~4.5 Ma ago at the TAMMAR segment. Based on joint observations of seismic travel time tomography and MBA, the SK segment is interpreted to show the same behavior in the migration of its melting region and mantle upwelling. However, this region expanded toward the north and the migration has stopped, as indicated by the wide axial valley and OCC formation at its northern end.

As inferred in previous gravity studies, we suggest that the source of observed ridge propagation has its origin within the mantle and is linked to a sudden increase in either the dimensions of the melt supply region or a transient increase in the fertility of the asthenosphere south of Kane transform. The migration speed of the segment center is slower than the propagation rate of the segment. This implies that the center of the mantle upwelling region also migrates as the segment grows along axis. The preferred expansion direction may be influenced by the distance to "cold" mantle zones. As previously suggested, large offset discontinuities act as more significant barriers to ridge propagation. The larger the offset at a fracture zone, the stronger the lithospheric barrier to ridge migration and the geometric influence on subridge diapirism.

We propose a connection between both propagating segments (TS and SK) at a larger scale within the asthenosphere, in the melting zone to form a long, highly magmatically active macrosegment, here called the TAMMAR-Kane Macrosegment.

In this region, the growth of mantle upwelling and melt supply became large enough to terminate the previously long-lived 21°40′ TF. This is a good example of this rarely observed phenomenon. As a consequence, detachment faulting stopped. In contrast, in the center of the TKMS detachment faulting stopped due to reduced melt supply. The center of the TKMS has had relatively uniform crustal accretion over the past 8 Myr with alternating OCC formation to both sides of its ridge axis.

Several basic questions remain unanswered: How long will the TAMMAR segment continue to propagate? Will the segment center and its associated zone of enhanced mantle upwelling still migrate toward the south even after the segment has stopped its along-axis growth? Does the TKMS break up during continuous separation of the magma productivity zones and as a result does the southwards expansion stop? Does asymmetric spreading favor the faster-spreading ridge flank for OCC formation? We hope that comparative study between this and other examples of these processes can shed further light on the mantle and crustal controls on ridge propagation at a median-valley spreading center.

Acknowledgments
The COSTMAR experiment was funded by the Deutsche Forschungsgemeinschaft (DFG) grants Mo 961/5-1, Ra 925/5-1, and Gr 1964/8-2 + 8-3. The authors thank their colleagues who supported the work during the cruise and give particular thanks to the ship's master Captain Kull and the crew of R/V *Meteor*. Generic Mapping Tools (Wessel & Smith, 1998) were used to produce the basis for the figures. We thank two anonymous reviewers for their detailed and helpful reviews of the manuscript. Seismic data are available on request from the first author or via https://portal.geomar.de/.

References

Birch, F. (1961). The velocity of compressional waves in rocks to 10 kilobars. Part 2. *Journal of Geophysical Research*, *66*, 2199–2224. https://doi.org/10.1029/JZ066i007p02199

Blackman, D. K., Canales, J. P., & Harding, A. (2009). Geophysical signatures of oceanic core complexes. *Geophysical Journal International*, *178*(2), 593–613. https://doi.org/10.1111/j.1365-246X.2009.04184.x

Bonatti, E., Ligi, M., Brunelli, D., Cipriani, A., Fabretti, P., Ferrante, V., … Ottolini, L. (2003). Mantle thermal pulses below the Mid-Atlantic Ridge and temporal variations in the formation of oceanic lithosphere. *Nature*, *423*(6939), 499–505. https://doi.org/10.1038/nature01594

Briais, A., Aslanian, D., Geli, L., & Ondréas, H. (2002). Analysis of propagators Along the Pacific-Antarctic ridge: Evidence for triggering by kinematic changes. *Earth and Planetary Science Letters*, *199*(3-4), 415–428. https://doi.org/10.1016/S0012-821X(02)00567-8

Brozena, J. M., & White, R. S. (1990). Ridge jumps and propagations in the South Atlantic Ocean. *Nature*, *348*(6297), 149–152. https://doi.org/10.1038/348149a0

Buck, W. R., Einarsson, P., & Brandsdottir, B. (2006). Tectonic stress and magma chamber size as controls on dike propagation: Constraints from the 1974-1989 Krafla rifting episode. *Journal of Geophysical Research*, *111*, B12404. https://doi.org/10.1029/2005JB003879

Buck, W. R., Lavier, L. L., & Poliakov, A. N. (2005). Modes of faulting at mid-ocean ridges. *Nature*, *434*(7034), 719–723. https://doi.org/10.1038/nature03358

Canales, J. P. (2010). Small-scale structure of the Kane oceanic core complex, Mid-Atlantic Ridge 23°30′N, from waveform tomography of multichannel seismic data. *Geophysical Research Letters*, *37*, L21305. https://doi.org/10.1029/2010GL044412

Canales, J. P., Detrick, R. S., Lin, J., & Collins, J. A. (2000). Crustal and upper mantle seismic structure beneath the rift mountains and Across a nontransform offset at the Mid-Atlantic Ridge (35°N). *Journal of Geophysical Research*, *105*, 2699–2719. https://doi.org/10.1029/1999JB900379

Cann, J. R., Smith, D. K., Escartin, J., & Schouten, H. (2015). Tectonic evolution of 200 km of Mid-Atlantic Ridge over 10 million years: Interplay of volcanism and faulting. *Geochemistry, Geophysics, Geosystems*, *16*, 2303–2321. https://doi.org/10.1002/2015GC005797

Carbotte, S., Welch, S. M., & Macdonald, K. C. (1991). Spreading rates, rift propagation and fracture zone offset histories during the past 5 my on the Mid-Atlantic Ridge: 25°-27°30′S and 31°-34°S. *Marine Geophysical Researches*, *13*(1), 51–80. https://doi.org/10.1007/BF02428195

Carlson, R. L. (1998). Seismic velocities in the uppermost oceanic crust: Age dependence and the fate of layer 2A. *Journal of Geophysical Research*, *95*, 9153–7077. https://doi.org/10.1029/JB095iB06p09153

Carlson, R. L., & Herrick, C. N. (1990). Densities and porosities in the oceanic crust and their variations with depth and age. *Journal of Geophysical Research*, *95*, 9153–9170. https://doi.org/10.1029/JB095iB06p09153

Cheadle, M., & Grimes, C. (2010). To fault or not to fault. *Nature Geoscience*, *3*(7), 454–456. https://doi.org/10.1038/ngeo910

Cormier, M. H., & Macdonald, K. C. (1994). East Pacific rise 18°–19°S: Asymmetric spreading and ridge reorientation by ultra-fast migration of axial discontinuities. *Journal of Geophysical Research*, *99*, 543–564. https://doi.org/10.1029/93JB02382

Cushman, B., Sinton, J., & Ito, G. (2004). Glass compositions, plume-ridge interaction, and hydrous melting along the Galápagos spreading center, 90.5°W to 98°W. *Geochemistry, Geophysics, Geosystems*, *5*, Q08E17. https://doi.org/10.1029/2004GC000709

Dannowski, A., Grevemeyer, I., Morgan, J. P., Ranero, C. R., Maia, M., & Klein, G. (2011). Crustal structure of the propagating TAMMAR ridge segment on the Mid-Atlantic Ridge, 21.5°N. *Geochemistry, Geophysics, Geosystems*, *12*, Q07012. https://doi.org/10.1029/2011GC003534

Dannowski, A., Grevemeyer, I., Ranero, C. R., Ceuleneer, G., Maia, M., Morgan, J. P., & Gente, P. (2010). Seismic structure of an oceanic core complex at the Mid-Atlantic Ridge, 22°19′N. *Journal of Geophysical Research*, *115*, B07106. https://doi.org/10.1029/2009JB006943

Dick, H. J. B., Tivey, M. A., & Tucholke, B. E. (2008). Plutonic foundation of a slow-spreading ridge segment: Oceanic core complex at Kane Megamullion, 23°30′N, 45°20′W. *Geochemistry, Geophysics, Geosystems*, *9*, Q05014. https://doi.org/10.1029/2008GC001645

Gac, S., Tisseau, C., Dyment, J., & Goslin, J. (2006). Modelling the thermal evolution of slow-spreading ridge segments and their off-axis geophysical signature. *Geophysical Journal International*, *164*(2), 341–358. https://doi.org/10.1111/j.1365-246X.2005.02844.x

Gente, P., Ceuleneer, G., Dauteuil, O., Dyment, J., Honsho, C., Laverne, C., … Thebaud, R. (1996). On- and off-axis submersible investigations on an highly magmatic segment of the Mid-Atlantic Ridge (21°40′N): The TAMMAR cruise. *InterRidge News*, *5*(2), 27–31.

Gente, P., Pockalny, R., Durand, C., Maia, M., Deplus, C., Mével, C., … Laverne, C. (1995). Characteristics and evolution of the segmentation of the Mid-Atlantic Ridge between 20°N and 24°N during the last 10 million years. *Earth and Planetary Science Letters*, *129*(1-4), 55–71. https://doi.org/10.1016/0012-821X(94)00233-O

Grevemeyer, I., & Weigel, W. (1996). Seismic velocities of the uppermost igneous crust versus age. *Geophysical Journal International*, *124*(2), 631–635. https://doi.org/10.1111/j.1365-246X.1996.tb07041.x

Grevemeyer, I., & Weigel, W. (1997). Increase of seismic velocities in upper oceanic crust: The "superfast" spreading East Pacific Rise at 14°14′S. *Geophysical Research Letters*, *21*, 2163–2166. https://doi.org/10.1029/94GL01913

Hey, R. N. (1977). A new class of pseudofaults and their bearing on plate tectonics: A propagating rift model. *Earth and Planetary Science Letters*, *37*(2), 321–325. https://doi.org/10.1016/0012-821X(77)90177-7

Hey, R. N., Duennebier, F. K., & Morgan, W. J. (1980). Propagating rifts on mid-ocean ridges. *Journal of Geophysical Research*, *85*, 3647–3658. https://doi.org/10.1029/JB085iB07p03647

Hey, R. N., Kleinrock, M. C., Miller, S. P., Atwater, T. M., & Searle, R. C. (1986). Sea beam/deep-tow investigation of an active oceanic propagation rift system, Galapagos 95.5°W. *Journal of Geophysical Research*, *91*, 3369–3393. https://doi.org/10.1029/JB091iB03p03369

Hey, R. N., Menard, H. W., Atwater, T. M., & Caress, D. W. (1988). Changes in direction of seafloor spreading revisited. *Journal of Geophysical Research*, *93*, 2803–2811. https://doi.org/10.1029/JB093iB04p02803

Kahle, R. L., Tilmann, F., & Grevemeyer, I. (2016). Crustal structure and kinematics of the TAMMAR propagating rift system on the Mid-Atlantic Ridge from seismic refraction and satellite altimetry gravity. *Geophysical Journal International*, *206*(2), 1382–1397. https://doi.org/10.1093/gji/ggw219

Karson, J. A. (1999). Geological investigation of a lineated massif at the Kane transform fault: Implications for oceanic core complexes. *Philosophical Transactions. Royal Society of London*, *357*(1753), 713–740. https://doi.org/10.1098/rsta.1999.0350

Kleinrock, M. C., Tucholke, B. E., Lin, J., & Tivey, M. A. (1997). Fast rift propagation at a slow-spreading ridge. *Geology*, *25*(7), 639–642. https://doi.org/10.1130/0091-7613(1997)025%3C0639:FRPAAS%3E2.3.CO;2

Korenaga, J., Holbrook, W. S., & Dahl-Jensen, T. (2000). Crustal structure of the southeast Greenland margin from joint refraction and reflection seismic tomography. *Journal of Geophysical Research*, *105*, 21,591–21,614. https://doi.org/10.1029/2000JB900188

Korenaga, J., Holbrook, W. S., Detrick, R. S., & Kelemen, P. B. (2001). Gravity anomalies and crustal structure at the southeast Greenland margin. *Journal of Geophysical Research*, *106*, 8853–8870. https://doi.org/10.1029/2000JB900416

Lin, J., Purdy, G. M., Schouten, H., Sempere, J. C., & Zervas, C. (1990). Evidence from gravity data for focused magmatic accretion along the Mid-Atlantic Ridge. *Nature*, *344*(6267), 627–632. https://doi.org/10.1038/344627a0

Macdonald, K. C., Fox, P. J., Perram, L. J., Eisen, M. F., Haymon, R. M., Miller, S. P., … Shor, A. N. (1988). A new view of the mid-ocean ridge from the behaviour of ridge-axis discontinuities. *Nature*, *335*(6187), 217–225. https://doi.org/10.1038/335217a0

Macdonald, K. C., Scheirer, D. S., & Carbotte, S. M. (1991). Mid-Ocean ridges: Discontinuities, segments and giant cracks. *Science*, *253*(5023), 986–994. https://doi.org/10.1126/science.253.5023.986

Maia, M., & Gente, P. (1998). Three-dimensional gravity and bathymetry analysis of the Mid-Atlantic Ridge between 20°N and 24°N: Flow geometry and temporal evolution of the segmentation. *Journal of Geophysical Research*, *103*, 951–974. https://doi.org/10.1029/97JB01635

Maia, M., Sichel, S., Briais, A., Brunelli, B., Ligi, M., Ferreira, N., … Oliveira, P. (2016). Extreme mantle uplift and exhumation along a transpressive transform fault. *Nature Geoscience*, *9*(8), 619–623. https://doi.org/10.1038/NGEO2759

Menard, H. W., & Atwater, T. (1968). Changes in direction of sea floor spreading. *Nature*, *219*(5153), 463–467. https://doi.org/10.1038/219463a0

Morgan, J. P., & Parmentier, E. M. (1985). Causes and rate-limiting mechanisms of ridge propagation: A fracture mechanics model. *Journal of Geophysical Research*, *90*, 8603–8612. https://doi.org/10.1029/JB090iB10p08603

Morgan, J. P., & Sandwell, D. T. (1994). Systematics of ridge propagation south of 30°S. *Earth and Planetary Science Letters*, *121*(1-2), 245–258. https://doi.org/10.1016/0012-821X(94)90043-4

Moser, T. J. (1991). Shortest path calculation of seismic rays. *Geophysics*, *56*(1), 59–67. https://doi.org/10.1190/1.1442958

Moser, T. J., Nolet, G., & Snieder, R. (1992). Ray bending revisited. *Bulletin of the Seismological Society of America*, *82*, 259–288.

Müller, R. D., Sdrolias, M., Gaina, C., & Roest, W. R. (2008). Age, spreading rates and spreading symmetry of the world's ocean crust. *Geochemistry, Geophysics, Geosystems*, *9*, Q04006. https://doi.org/10.1029/2007GC001743

Niu, Y., Bideau, D., Hékinian, R., & Batiza, R. (2001). Mantle composisitional control on the extend of mantle melting, crust production, gravity anomaly, ridge morphology, and ridge segmentation: A case study at the Mid-Atlantic Ridge 33-35°N. *Earth and Planetary Science Letters*, *186*(3-4), 383–399. https://doi.org/10.1016/S0012-821X(01)00255-2

Parsons, B., & Sclater, J. G. (1977). An analysis of the variation of ocean floor bathymetry and heat flow with age. *Journal of Geophysical Research*, *82*, 803–827.

Ranero, C. R., Reston, T. J., Belykh, I., & Gnibidenko, H. (1997). Reflective oceanic crust formed at a fast-spreading center in the Pacific. *Geology*, *25*(6), 499–502. https://doi.org/10.1130/0091-7613(1997)025%3C0499:ROCFAA%3E2.3.CO;2

Reston, T. J., Ranero, C. R., & Belykh, I. (1999). The structure of ocean crust at fast spreading rates: Constraints from the cretaceous of the NW Pacific. *Journal of Geophysical Research*, *104*, 629–644. https://doi.org/10.1029/98JB02640

Sandwell, D. T., & Smith, W. H. F. (1997). Marine gravity anomaly from Geosat and ERS-1 satellite altimetry. *Journal of Geophysical Research*, *102*, 10,039–10,054. https://doi.org/10.1029/96JB03223

Schouten, H., Dick, H. J. B., & Klitgord, K. D. (1987). Migration of mid-ocean ridge volcanic segments. *Nature*, *326*(6116), 835–839. https://doi.org/10.1038/326835a0

Searle, R. C., & Hey, R. N. (1983). GLORIA observations of the propagating rift at 95.5°W on the Cocos-Nazca spreading center. *Journal of Geophysical Research*, *88*, 6433–6447. https://doi.org/10.1029/JB088iB08p06433

Seher, T., Crawford, W. C., Singh, S. C., Cannat, M., Combier, V., & Dusunur, D. (2010). Crustal velocity structure of the lucky strike segment of the Mid-Atlantic Ridge at 37°N from seismic refraction measurements. *Journal of Geophysical Research*, *115*, B03103. https://doi.org/10.1029/2009JB006650

Sempéré, J. C., Blondel, P., Briais, A., Fujiwara, T., Géli, L., Isezaki, N., … Rommevaux, C. (1995). The Mid-Atlantic Ridge between 29°N and 31°30′N in the last 10 Ma. *Earth and Planetary Science Letters*, *130*(1-4), 45–55. https://doi.org/10.1016/0012-821X(94)00259-2

Sempéré, J. C., Lin, J., Brown, H. S., Schouten, H., & Purdy, G. M. (1993). Segmentation and morphotectonic variations along a slow-spreading center: Mid-Atlantic Ridge (24°00′N-30°40′N). *Marine Geophysical Researches*, *15*(3), 153–200. https://doi.org/10.1007/BF01204232

Shearer, P. M. (1988). Cracked media, Poisson's ration and the structure of the upper oceanic crust. *Geophysical Journal*, *92*(2), 357–362. https://doi.org/10.1111/j.1365-246X.1988.tb01149.x

Smith, D. K., Escartin, J., Cannat, M., Tolstoy, M., Fox, C. G., Bohnenstiel, D. R., & Basin, S. (2003). Spatial and temporal distribution of seismicity along the Mid-Atlantic Ridge (15–35°N). *Journal of Geophysical Research*, *108*(B3), 2167. https://doi.org/10.1029/2002JB001964

Smith, W. H. F., & Sandwell, D. T. (1997). Global seafloor topography from satellite altimetry and ship depth soundings. *Science*, *277*, 1957–1962.

Stevenson, J. M., Hildebrand, J. A., & Zumberge, M. A. (1994). An ocean bottom gravity study of the southern Juan de Fuca ridge. *Journal of Geophysical Research*, *99*(B3), 4875–4888. https://doi.org/10.1029/93JB02076

Thibaud, R., Gente, P., & Maia, M. (1998). A systematic analysis of the Mid-Atlantic Ridge morphology and gravity between 15°N and 40°N: Constraints of the thermal structure. *Journal of Geophysical Research*, *103*, 24,223–24,243. https://doi.org/10.1029/97JB02934

Tolstoy, M., Harding, A. J., & Orcutt, J. A. (1993). Crustal thickness on the Mid-Atlantic Ridge: Bull's eye gravity anomalies and focused accretion. *Science*, *262*(5134), 726–729. https://doi.org/10.1126/science.262.5134.726-9

Toomey, D. R., Solomon, S. C., & Purdy, G. M. (1988). Microearthquakes beneath the median valley of the Mid-Atlantic Ridge near 23°N: Tomography and tectonics. *Journal of Geophysical Research*, *93*, 9093–9112. https://doi.org/10.1029/JB093iB08p09093

Tucholke, B. E., Behn, M. D., Buck, W. R., & Lin, J. (2008). Role of melt supply in oceanic detachment faulting and formation of meagmullions. *Geology*, *36*(6), 455–458. https://doi.org/10.1130/G24639A.1

Wessel, P., & Smith, W. H. F. (1998). New improved version of the generic mapping tools released. *Eos, Transactions American Geophysical Union*, *79*(47), 579. https://doi.org/10.1029/98EO00426

White, R. S., McKenzie, D., & O'Nions, R. K. (1992). Oceanic crustal thickness from seismic measurements and rare earth element inversions. *Journal of Geophysical Research*, *97*, 19,683–19,715. https://doi.org/10.1029/92JB01749

Whitmarsh, R. B. (1978). Seismic refraction studies of the upper igneous crust in the North Atlantic and porosity estimates for layer 2. *Earth and Planetary Science Letters*, *37*(3), 451–464. https://doi.org/10.1016/0012-821X(78)90061-4

Wiener, N. (1949). *Extrapolation, interpolation, and smoothing of stationary time series*. New York: John Wiley.

Wilson, D. S., Hey, R. N., & Nishimura, C. (1984). Propagation as a mechanism of reorientation of the Juan de Fuca ridge. *Journal of Geophysical Research*, *89*, 9215–9225. https://doi.org/10.1029/JB089iB11p09215

Wilson, S. C., Murton, B. J., & Taylor, R. N. (2013). Mantle composition controls the development of an oceanic core complex. *Geochemistry, Geophysics, Geosystems*, *14*, 979–995. https://doi.org/10.1002/ggge.20046